SUPPORTING INFORMATION

Platinum-Nickel Nanowires and Nanotubes Arrays as Carbon-free Cathodes for the PEM Fuel Cell

Othman. Lagrichi[‡†], Laure Guétaz[‡], Olivier Sicardy[‡], Denis Buttard[†], Arnaud Morin[‡]

[‡]Univ. Grenoble Alpes, CEA, Liten, DEHT, STP, F-38000 Grenoble, France

[†] Univ. Grenoble Alpes, CEA, IRIG, Pheliqs, SiNaPS, F-38000 Grenoble, France

*Corresponding author: arnaud.morin@cea.fr

SI 1: Scheme of the monocell assembly for both a) Pt/C and b) PtNi electrodes:

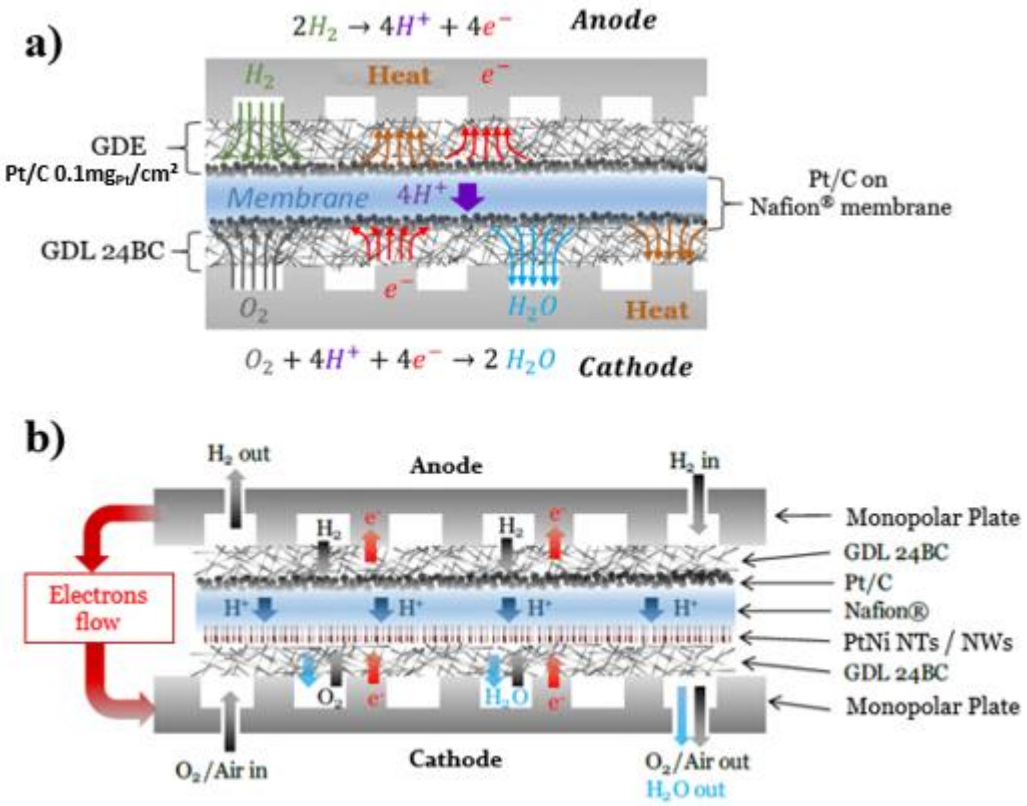

Figure S1. Schematic images of **a)** a cross-sectional schematic illustration of the mono-cell assembly used in a differential cell test and **b)** the single-cell test cell with Platinum nanotubes/nanowires embedded on a Nafion® membrane on the cathode side and a conventional Pt/C catalyst on the anode side (0.1 mg_{Pt}/cm^2).

SI 2: MEA Break-in effect

The performance of the MEA significantly improved after conditioning, as we can clearly see in *figure S2*. Some researchers have attributed this increase in performance to changes in the MEA microstructures [3][3]. From our viewpoint, this increase might be related to the ionomer swelling and reorganization, removal of pollutants, reorganization of the catalytic sites, or to the reorientation of active facets of Pt. It is worth noting that at 0.65V, the current density improved after the break-in and ohmic loss correction from 0,35 A/cm^2_{geo} to 0.62 A/cm^2_{geo}. The OCV value reads in this case: $\mathbf{E_{OCV} = 0,928\ V}$.

The figure below displays the polarization curve at the aforementioned conditions after the ohmic drop correction.

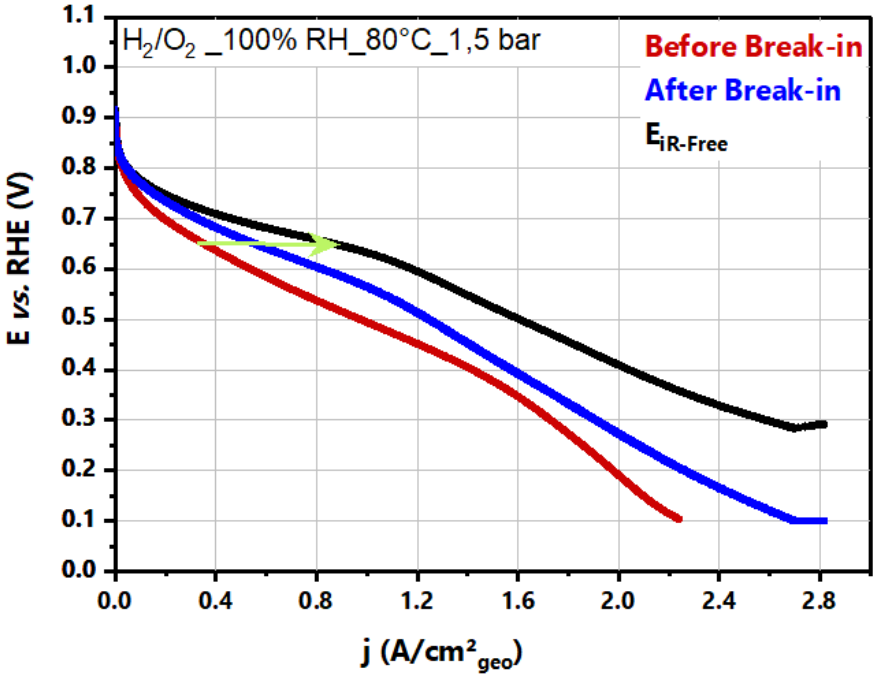

Figure S2. Measured polarization curve as a function of geometrical current density at T_{cell}=80°C, 100% RH (dew points), wet H_2/O_2 gas flow, and a total pressure 1.5 bar. **Red-curve**: original un-corrected polarization curve, **Blue-curve**: polarization curve after the break-in, and **Black-curve**: The resistance-corrected cell voltage ($E_{iR\text{-}free}$). The homemade catalyst layer is made of Pt/C ($0.1 mg_{Pt}/cm^2$ - $0.035 mg_{Pt}/cm^2$ at the anode and the cathode, respectively).

SI 3: Cyclic voltammograms (CVs) were measured after the break-in process at 40°C and 80°C at 100% RH under a pressure of 1 bar. Since the available ECSA might be small due to the Pt low-loading, we have recorded the CVs at a scan rate of 200 mV/s to be able to measure it: Varying the working electrode's potential between 0.1 to 1.2 V_{RHE}, assuming that the counter-electrode potential is fixed at 0 V_{RHE}.

The current is measured and recorded during the scan. After that, the active electrochemical surface area (ECSA) was averaged from the hydrogen underpotential deposition (H_{UPD}) region of cyclic voltammograms (H-desorption charges between 0.1 and 0.4 V_{RHE}).

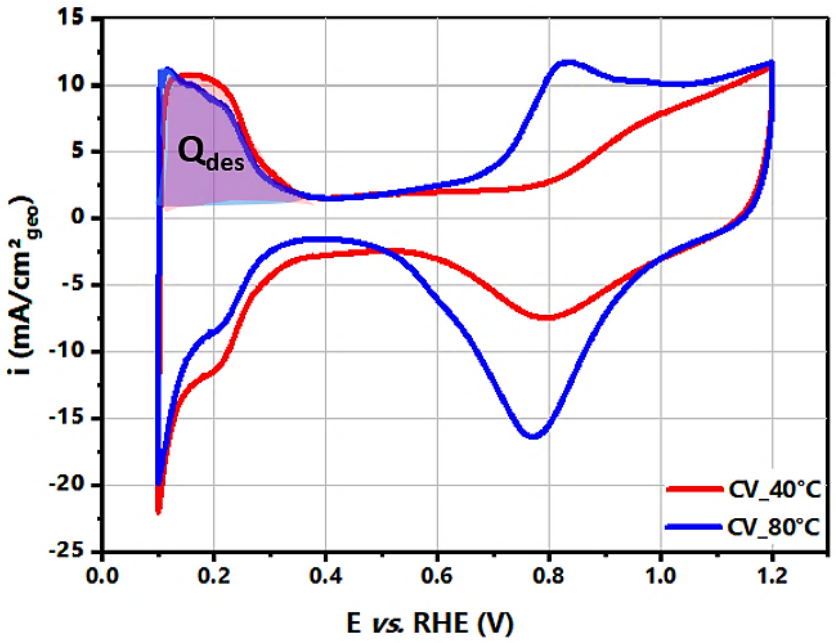

Figure S3. Cyclic voltammogram in fully humidified H_2/N_2 of the Pt/C electrode with low Pt-loading at the cathode (35$\mu g_{Pt}/cm^2$). Data were recorded at scan-speed of 200mV/s, 40°C (red curve), and 80°C (blue curve) with a 1 bar total pressure. The blue and red areas (in the 0.1 – 0.4 V_{RHE} potential range) correspond to hydrogen desorption.

SI 4: Double anodization process

The system consists of: **i/** the cell with a mechanical holder for the sample, **ii/** a circular Platinum-Iridium gauze acting as counter-electrode, **iii/** a stirrer to assure solution homogeneity which guarantees stable conditions during anodization and to remove hydrogen bubbles effectively, and **iv/** a computer-controlled *Keithley™ 2612A* Source meter combined with *TSP®Express* software. All components were mounted in a closed metal box for safety issues.

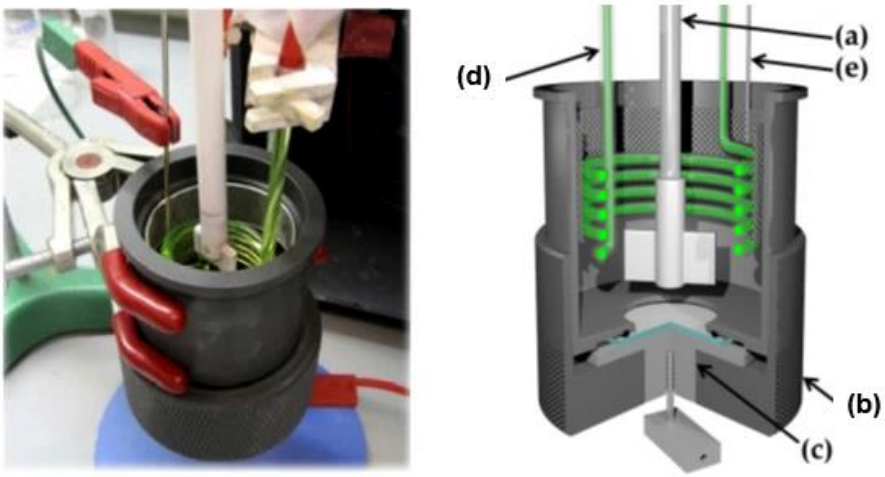

Figure S4. Electrochemical cell setup used for anodizing aluminum on p-type silicon substrate (Left picture) and 3D model of the PVC cell (right picture) composed of: **a)** Stirrer, **b)** PVC core, **c)** Metal

cap that ensures electrical contact and mechanical cohesion between the cell and the sample (electrode), **d)** Flowing cooling Liquid system to adjust the temperature of the electrolyte, **e)** Cylindrical platinum gauze as counter-electrode.

The sample (Al/Si substrate) is placed on the backside of the PVC cell and electrically contacted by a stainless-steel piece whose role is to press the front side of the substrate, while the front side (where the aluminum layer has been deposited) is in contact with the acidic solution. The Platinum-Iridium cylindrical gauze's relevance (*i.e.*, counter electrode) is to facilitate the escape of hydrogen bubbles and removes local heat on the surface and allows a homogenous diffusion of anions into pore channels. It is placed into the electrolyte, far from the sample, to ensure parallel electric field lines on the entire surface of the Al surface. Finally, a cap is screwed under the cell to assure its mechanical cohesion.

To have more precise control of the anodization process, the voltage was applied by *Keithley™ 2612A* power supply. The electric current was monitored and recorded using the same instrument. The apparatus was controlled by a home-built computer script. The control of the experimental conditions is critical to maintaining a stable and homogeneous medium during anodization.

First and foremost, the samples (Al/Si) are cleaned in acetone then isopropanol to remove microparticles and organic contaminations. After mounting the anodizing setup, first anodization was carried out in 3%wt oxalic acid at 34 V at room temperature (23°C). The voltage, temperature, and acid concentration have been adapted to the final pore's size (50-55nm in diameter). Such parameters have a direct effect on the pore size, interpore distance, thickness of the barrier layer, and the length of pores (*i.e.*, thickness). As previously evidenced, surface defects promote the growth of nanopores on the surface of aluminum. A large number of small pores are initiated from these concavities. The recorded Time-current curve at constant voltage aims to tracking the evolution of anodization process and displays 3 different stages as shown in *figure S5* below.

Figure S5 shows the different stages of the evolution of anodization process:

-Stage I: the growth of a non-porous oxide on the surface of aluminum in addition to its native oxide naturally present on the surface. The total resistance of the system increases, whereas the current decreases.

- **Stage II:** The beginning of aluminum oxide local dissolution. The pores grow preferentially over the surface defects that locally (*i.e.*, where the electric field

concentrates), allowing the diffusion of Al^{3+} and O^{2-} ions through the compact oxide layer, thus increasing the oxidation current.

- **Stage III:** A permanent anodizing regime marks this phase. The aluminum oxidation current and the total ohmic resistance of the system remain constant because of the steady-state between the dissolution of alumina and aluminum's oxidation.

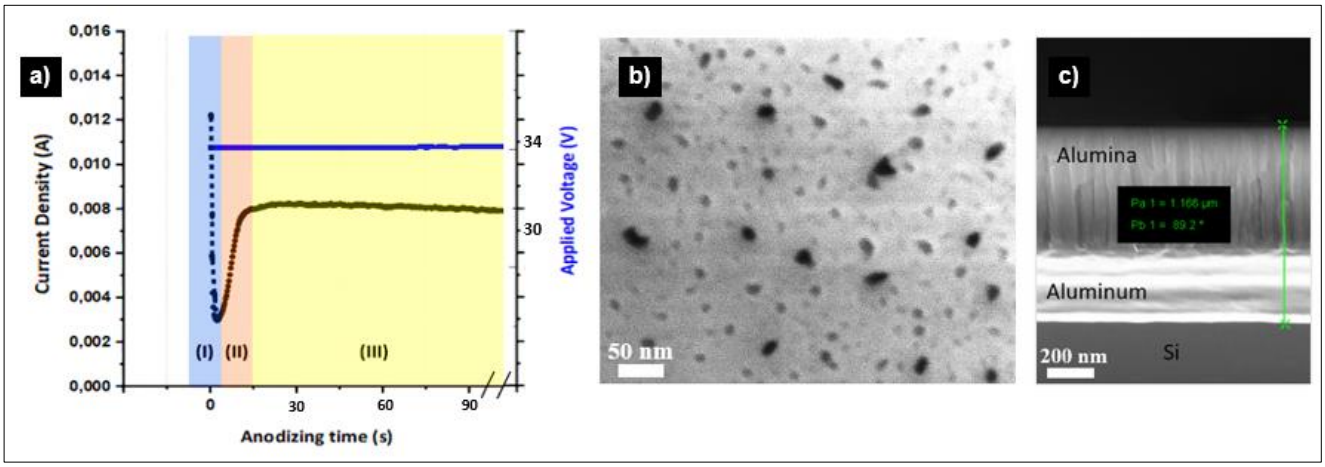

Figure S5. Schematic diagram of **a)** the evolution of current (j) vs. time (t) curve for one-step anodization in potentiostatic regime, for an aluminum/silicon (1 µm) sample anodized at 34 V in 3w% Oxalic acid at 23°C. The blue plot refers to the applied constant voltage of 34 V; the black plot refers to the evolution of the current density over time *(more details about every stage are expressed in Supporting Information (SI 1))*, **b)** SEM top-view of the resulting pores after the first anodization, and **c)** a SEM cross-section view of anodized alumina and the remaining aluminum at the bottom, attached to Si substrate.

The next step consists of wet and isotropic etching in 5%wt orthophosphoric solution at 35°C to achieve complete removal of the anodized alumina with irregular pores arrays, leaving pore imprints on the surface of residual aluminum as illustrated in *figure S6* below. The bowl-like nanostructure after etching is not due to a preferential direction of etching with orthophosphoric acid. This shape corresponds to the geometry of the bottom of the pore after the first anodization process. It is revealed after isotropic etching process which must be precisely controlled to keep this footprint after the first anodization. Such nanobowls are used as a precursor during the second anodization for the growth of more regular pores arrays hexagonally ordered.

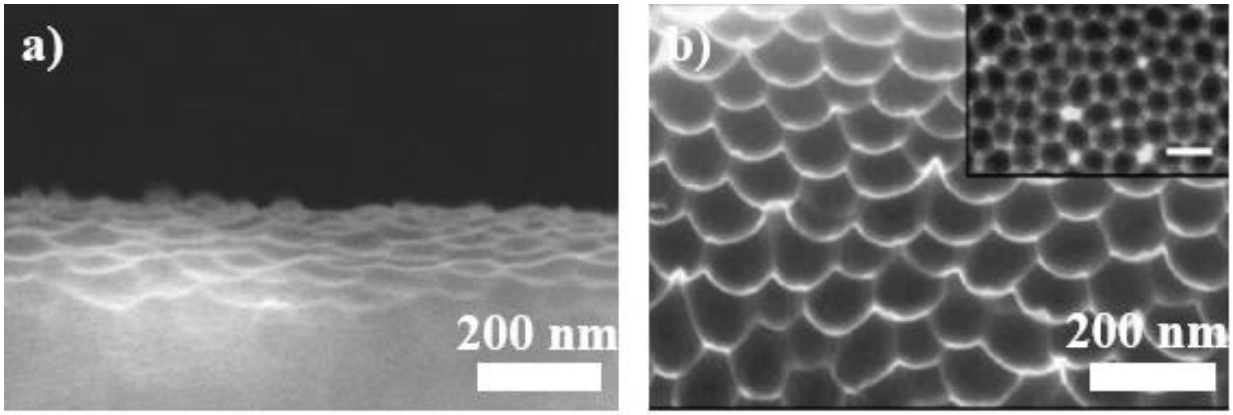

Figure S6. Scanning electron microscopy micrographs of **a)** aluminum nanobowls-like surface after i/ first step anodization of aluminum thin film (1 µm) on a silicon substrate, and ii/ first etching in 5%wt Orthophosphoric acid at 35°C as obtained in our experiment; **b)** tilted-view scanning electron microscopy image of an Al foil with nanobowl surface patterns reprinted from reference **Erreur ! Source du renvoi introuvable.** for comparison to literature.

Later, a second anodization was carried out at the same conditions during which the electrical field is concentrated on the remaining footprints, and thus improving the surface organization of nanopores. After the double anodization, the pores' organization depends mainly on the first anodization's duration, where the hexagonal arrays are well defined and offering better control of the structure. If the second anodization is not interrupted in time (as illustrated above on *stage IV*, *figure 8*), we observe a total peel-off (detachment) of the alumina membrane layer from the silicon substrate and the oxidation of the latter. *Stage IV* displays to a drop of the current (*i.e.*, increase of ohmic resistance) referring to the end of the anodization process (reaching Si interface).

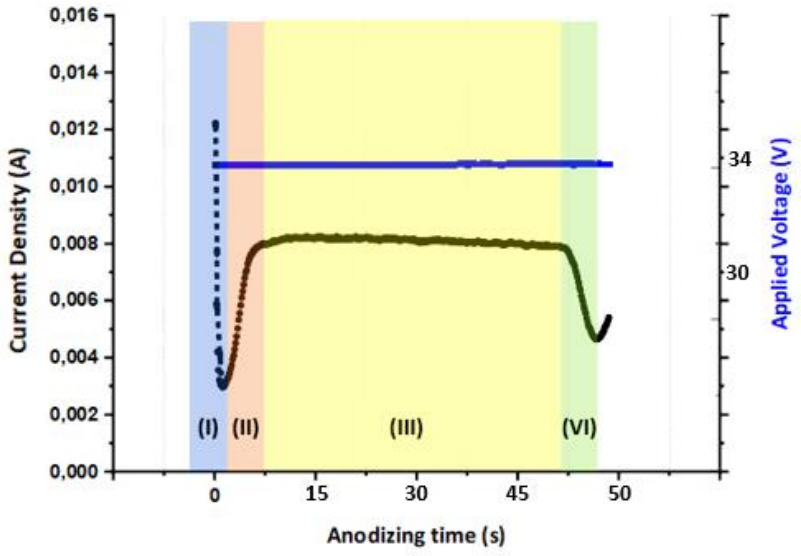

Figure S7. Schematic diagram of the evolution of current (j) *vs.* time (t) curve for one-step anodization in potentiostatic regime, for an aluminum/silicon (1 µm) sample anodized at 34 V in 3w% Oxalic acid at 23°C, with the four stages of anodization process.

The final step requires a second wet isotropic etching in 5%wt orthophosphoric solution at 35°C, for 8 minutes (adapted time to reach a pore's diameter of *ca.* 50-55 nm). It markedly leads to pore widening as well as the opening of the bottom barrier oxide layer (*see figure S8*) until reaching silicon substrate. The latter could undergo local oxidation first due to an extended period of anodization and second due to contact with acidic electrolytes.

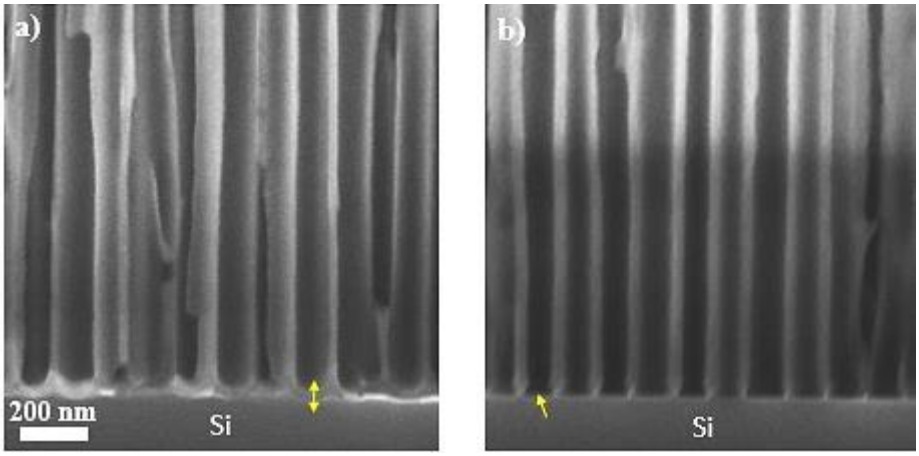

Figure S8. Cross-section scanning electron microscopy micrographs of porous aluminum oxide formed in 3%wt oxalic acid at 34 V **a)** before etching the barrier layer and **b)** after etching the barrier layer in 5%wt orthophosphoric acid at 35°C.

Also, we have followed the variation in initial pores diameter throughout many experiments held in 3%wt oxalic acid solution at different anodization voltages (24 V, 34 V, 54 V, and 64 V). According to the graph represented in *figure S9* below, it can be shown that the relation between the mean pore diameter and the anodizing voltage is linear, following the equation 1:

$$D_p = 1,13 + 0,47.U$$ Equation 1

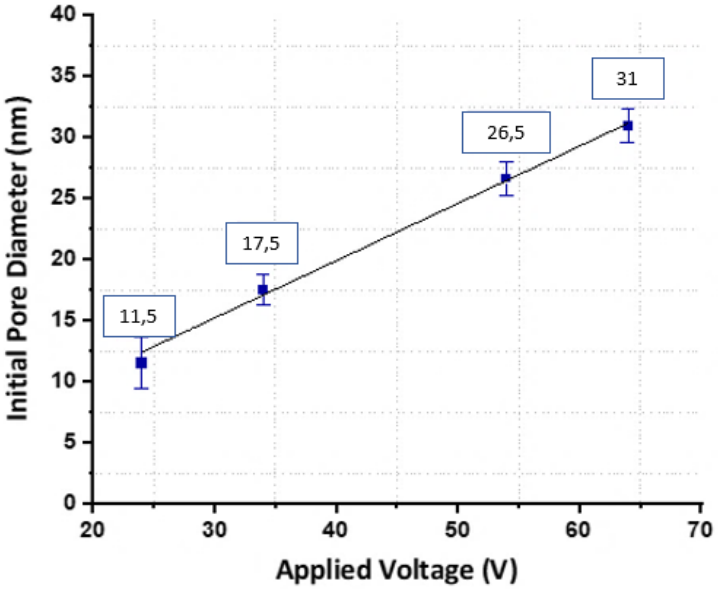

Figure S9. The evolution of mean initial pores diameter (D_p) as a function of the anodizing voltage of porous anodic aluminum oxide formed in 3%wt Oxalic acid at 24 V, 34 V, 54 V et 64 V at 23°C during the first anodization.

Stage IV displays to a drop of the current (*i.e.*, increase of ohmic resistance) referring to the end of the anodization process (reaching Si interface) as demonstrated in *figure S10*.

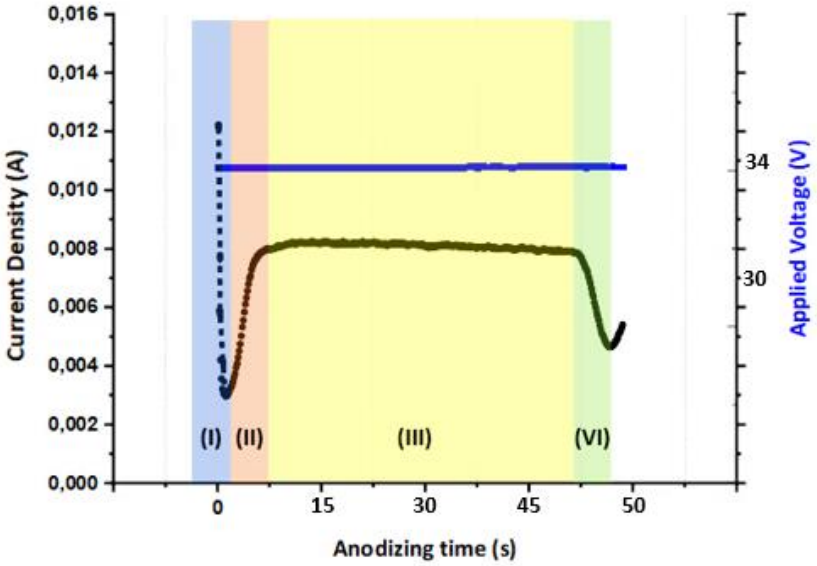

Figure S10. Schematic diagram of the evolution of current (j) *vs.* time (t) curve for one-step anodization in potentiostatic regime, for an aluminum/silicon (1 µm) sample anodized at 34 V in 3w% Oxalic acid at 23°C, with the four stages of anodization process.

SI 5: *Figure S11* below shows the evolution of pore diameter (D_p) as a function of pore wall etching time for porous AAO formed in 3%wt Oxalic acid ($H_2C_2O_4$). The plot is characterized by an inflection point, at which the slope of the curve changes. Pore wall oxide in the early stage is etched at a slightly higher rate than in the later stage. The retarded rate of etching in the later stage can be attributed to the relatively pure nature of the inner pore wall oxide compared to the less dense outer pore wall oxide due to the incorporation of anionic species [1].

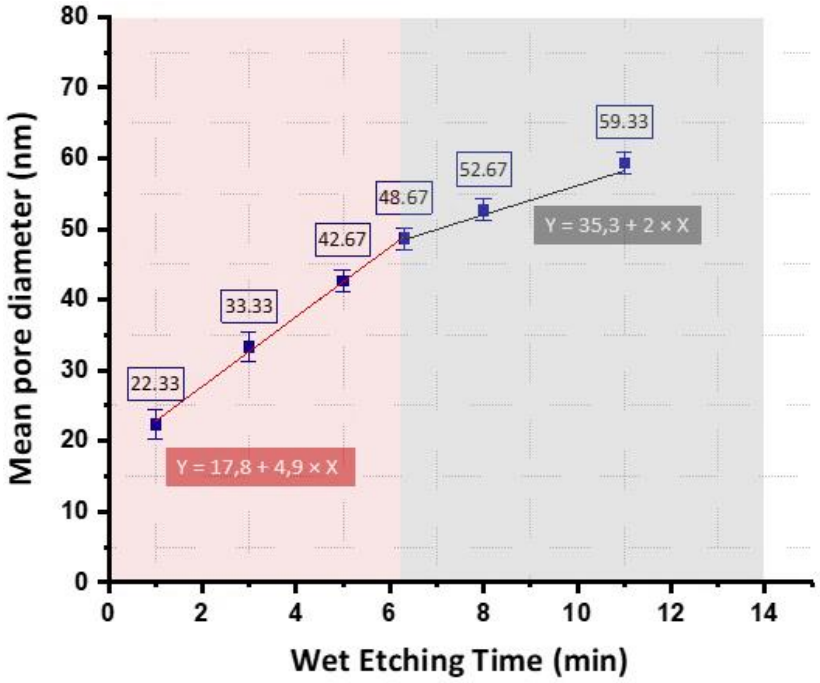

Figure S11. Evolution of mean pore diameter size (D_p) as a function of wet chemical etching time of porous anodic aluminum oxide formed in 3%wt oxalic acid at 34 V. Wet etching was performed in 5%wt orthophosphoric acid at 35°C.

SI 6: The deoxidation process was held into a *Primaxx Monarch 3 Module* that performs a vapor phase, selective, isotropic etch on the native silicon oxide. A constant flux of HF/N_2 (500sccm/1200sccm) along with alcohol flow at a maintained pressure of 75 torr is used to etch SiO_2, whose calibrated speed of etching is 11 nm/min.

We can clearly observe from *figure S12* the heterogeneous growth of NiNWs. This is attributed to the presence of thin native silicon oxide on the silicon surface at the bottom of the pores. Thus, after SiO_2 deoxidation, the deposition rate has been strikingly improved in terms of

height and filling ratio. Therefore, the removal of this layer was mandatory to a uniform NiNWs growth.

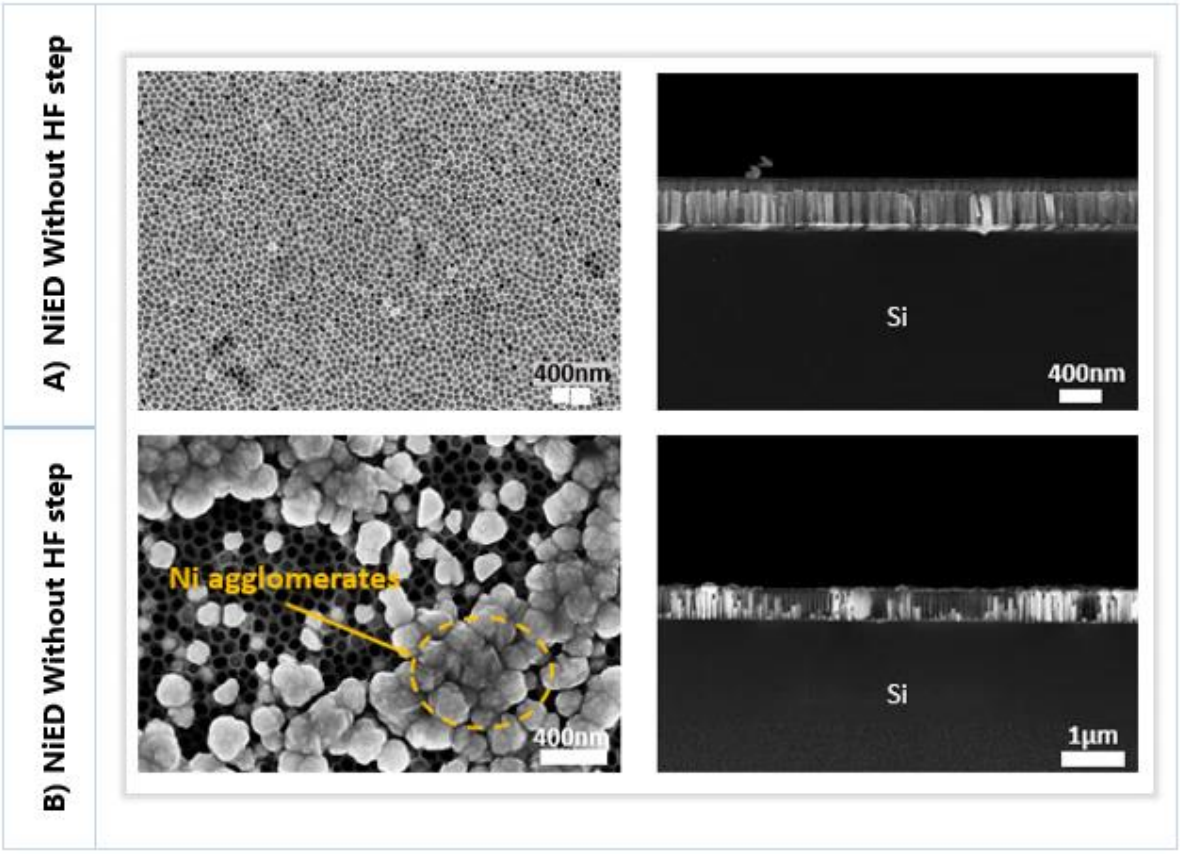

Figure S12. SEM micrographs of top and a cross-sectional view of NiNWs growth inside anodic aluminum oxide **A)** with HF deoxidation step and **B)** without HF deoxidation step.

SI 7: The prominent redox couples present in the solution and the concentration of the chemicals are reported in the *table S1 and S2* below:

Redox couples	E° (V *vs.* SHE)
$S_2O_2^{-8}$ /SO^{2-}	+2.01
O_2/H_2O	+1.23
H^+/H_2	0
Ni^{2+}/Ni	-0.257

Table S1. Standard electrode potential for redox couples present in a nickel solution.

The concentration of each component of the watts bath is displayed in *table 2* below:

Watts bath composition	
Nickel(II) sulfate - $NiSO_4$, $6H_2O$	220 to 300 g/L
Nickel(II) chloride - $NiCl_2$, $6H_2O$	35 to 65 g/L
Boric acid - H_3BO_3	35 to 45 g/L
Cathodic current density	0.02 A/cm² to 0.1 A/cm²
Temperature °C	35 à 55 °C
pH	3 to 5

Table S2. Composition of the Watts Bath as a nickel solution for nanowires electrodeposition.

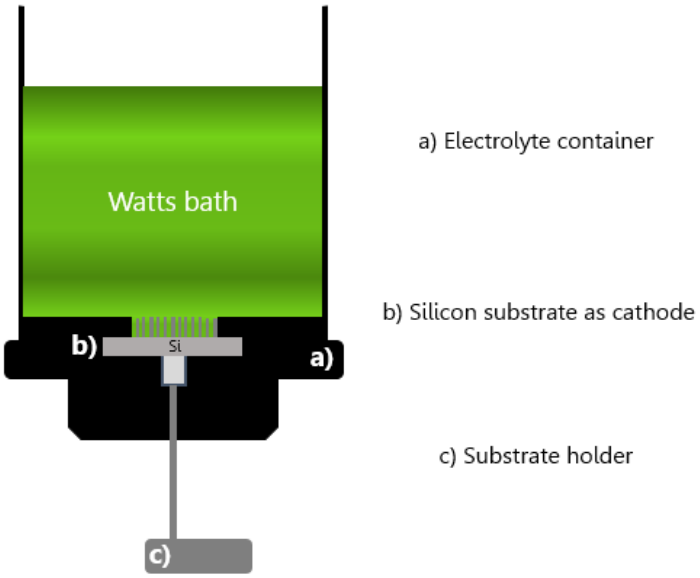

Figure S13. Schematic illustration of the electrochemical cell used for nickel nanowires electrodeposition on the AAO template. It is made of a) a electrolyte container, b) Anodic alumina oxide template on silicon substrate as cathode, and c) a substrate holder. The front side of the silicon wafer supporting the alumina membrane is used as the cathode, the rear side is for the electrical contact.

Sulfur is very complex from an electrochemical point of view. Sulfate ions are present both as an oxidizing and reducing agent. They are considered electronegative species, and they cannot react. They are only involved in current transport during ions migration [2].

Since the standard potential of the couple O_2/H_2O is higher than Ni^{2+}/Ni, the oxygen in the solution is reduced and may inhibit the cathodic reduction of nickel: we may have an added cathodic current which reduces the yield of Ni deposition.

Therefore, nitrogen was bubbled through the solution to keep the solution essentially free of oxygen. Also, considering the low standard potential of the couple Ni^{2+}/Ni compared to H^+/H_2, hydrogen emission is likely to occur in the electrolyte (H^+ protons reduction to H_2), leading to a decrease in the yield of Ni deposition: $I_{cathodic} = I_{H_2} + I_{Ni}$).

SI 8: Due to simultaneous hydrogen evolution during PED, the faradaic efficiency must be below 100%. For electrochemical calculations in this work, we will assume that faradaic efficiency is ~100%. NiNWs were deposited on silicon by square-wave galvanostatic pulses because of: **i/** the high aspect ratio of the cylindrical as evidenced before, **ii/** Keeping Ni^{2+} ions concentration nearly constant at the bottom of AAO pores, **iii/** constant current allows controlling the charge **Q** injected in the system assuming that there are no parasite reactions such as hydrogen production (*i.e.,* the amount of the deposited material or the thickness with a Ni(II) reduction yield equals to 100%) as follows:

$$\boldsymbol{Q = n_{e^-} \times n_{deposit} \times F} \qquad \text{Equation 2}$$

where:

n_{e^-}: is the number of electrons exchanged in the redox reaction;

$n_{deposit}$: the amount of substance (nickel) deposited in moles;

F: The Faraday constant, its currently accepted value is F = 96485 C/mol.

The Ni PED process was optimized during this work after several trials. Since we aim to reduce nickel, a constant negative current (I_{pulse-}) is applied on the cathode during a short time t_{on-} allowing the flow of a defined amount of charge Q leading to the reduction of nickel ions. This step is followed by a constant positive current (I_{pulse+}) during a short positive pulse t_{on+} follows to discharge the double-layer capacitance (*i.e.*, the interface between the conductive electrode and the adjacent nickel electrolyte, and to re-oxidize H_2 produced during t_{on-}). Subsequently, a relatively long-time t_{off} is applied to ensure ions' concentration to recover at the pore tips and for the deposition interfaces to be supplied with ions. *Figure S14* shows a schematic current-time transients pulses used for the pulsed electrodeposition of nickel alongside the PED parameters used in this experience. The total charge injected into the system is given as follow:

$$Q = I_{Pulse^-} \times t_{on^-} \times n_{Pulses}$$ Equation 3

where $n_{pulses-}$ is the total number of galvanic pulses.

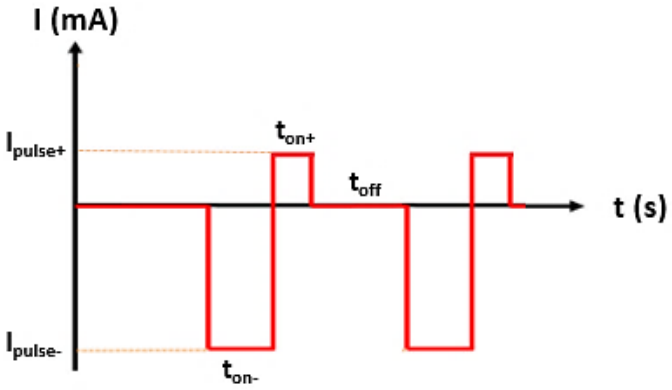

PED Parameters	Value
I_{pulse-}	80 mA/cm²
t_{on-}	52 ms
I_{pulse+}	30 mA/cm²
t_{on+}	10 ms
t_{off}	1 s

Figure S14: Schematic diagram of the time evolution of current during pulsed electrodeposition. Applied parameters in this thesis: Each high current pulse I_{pulse-} is applied for a time t_{on-} followed by a lower current pulse I_{pulse-} for a shorter time, then a concentration recovery time t_{off} of 1s. This process is repeated for 135, the experimental number of pulses.

In that regard, and prior to electrodeposition, it is possible to have a glimpse of the rate of filling of the pores, *i.e.*, the number of charges **Q** passing through the working electrode, relying on the porosity of anodic aluminum oxide mold. In the case of AAO small nanopores (**D_p=50-60 nm**, **e=400 nm**), the obtained porosity was estimated at **35%.**

The theoretical number of pulses n_{pulses} is calculated according to the desired length, thus to completely fill pores, using Faraday's law (*equation 4*):

$$n_{pulses} = \frac{\rho_M \times \%P \times e \times n_{e^-} \times F}{M_M \times t_{on-} \times I_{pulse^-}}$$ Equation 4

where:

Notation	Physical properties	Value
ϱ_M	Nickel density	8,902 g/cm^3 at 25°C
e	Alumina thickness	4.10^{-7} m
F	Faraday's constant	96485,33 A.s/mol
M_M	Ni molar mass	58,69 g/mol
%P	Porosity	35%
T_{on-}	Pulse time	0.052 s
I_{pulse-}	Current pulse	0,08 A/cm²

Table S3. Notations of physical properties and their standard value.

Using *equation 4*, the calculated number of pulses is 146 pulses, which is more or less in line with the experimental number of 135 pulses performed with a *Biologic*© Potentiostat and controlled with *EC-Lab*© software.

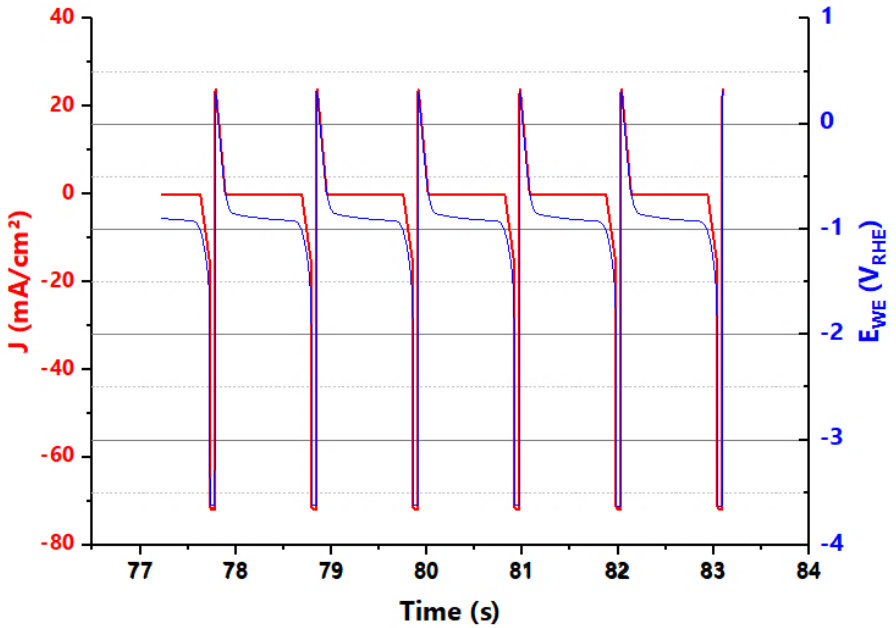

Figure S15. Experimental plot of the evolution of the current density (red plotting) and the potential response (blue plotting) over time during the nickel's pulsed electrodeposition.

When we exceed the right number of pulses, we notice and overflow of Ni growth and each nanowire emerges in the form of micrometric agglomerates, as displayed in *figure S16* below.

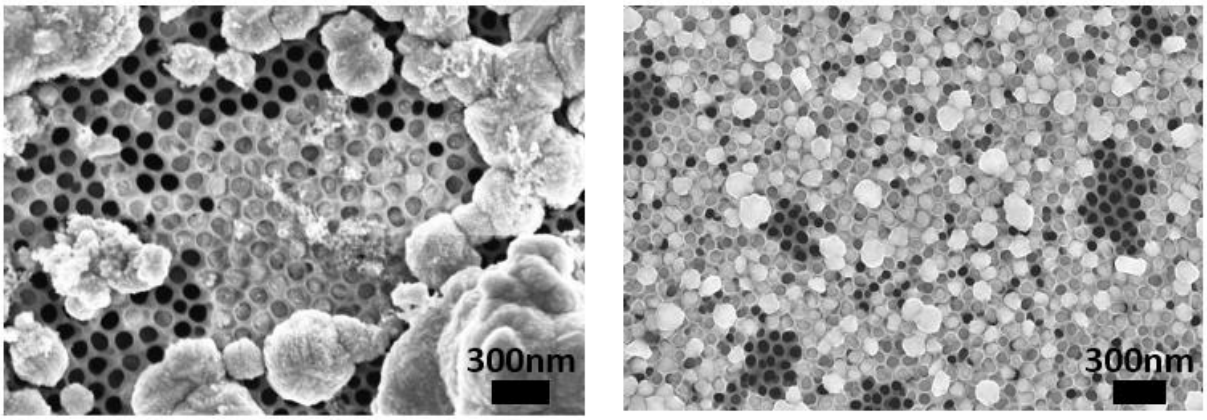

Figure S16. Top view scanning electron microscopy images (SEM) of nickel overgrowth on nanoporous aluminum oxide template

SI 9: The fabrication process of PtNiNWs and PtNiNTs:

Experiments held in this part strive to expand our understanding of combining/splitting galvanic displacement (GD) and acid leaching (AL) processes in a confined (NiNWs inside AAO) and a non-confined system (self-standing NiNWs on Si substrate):

- **i.** Reaction with the addition of HCl (combined GD and HCl): The Pt solution is diluted in a solution of HCl at different concentrations. NiNWs are exposed to this solution, and Ni atoms are exchanged with Pt atoms at a higher kinetic rate in the acid medium.
- **ii.** Reaction without the addition of HCl (splitted GD and AL): The Pt solution is diluted in ultra-pure water. The reaction of Pt deposition takes place at a slow rate. Pt tends to cover the surface of the NiNWs (Pt-shell@Ni-core). Later on, and once the process is over, the AL process is carried out after a thermal treatment to remove the excessive nickel in the core.

PtNiNWs fabrication:

Reproducible PtNiNWs were obtained after 8 minutes GD reaction at 35°C in K_2PtCl_4 solution with HCl 0.05 M, as shown in figure *figure S17*.

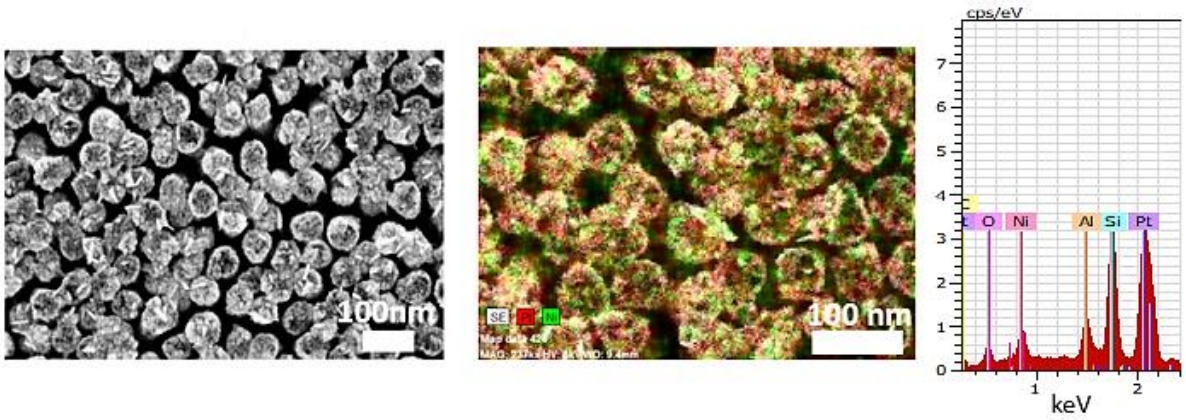

Figure S17: SEM top-view structural characterization coupled with EDX elemental mapping of PtNiNWs after exposing NiNWs to a K_2PtCl_4 solution in 0.05 M HCl at 35°C for 8 minutes.

For a deeper morphological analysis, the PtNiNWs were peeled off from the Si substrate and dispersed in a Copper transmission electron microscopy grid. The performed TEM-EDX quantitative microanalysis evidenced the formation of Pt_2Ni foam-like nanowires, displaying the distribution of Pt within the nickel as we can clearly observe in *figure S18* below.

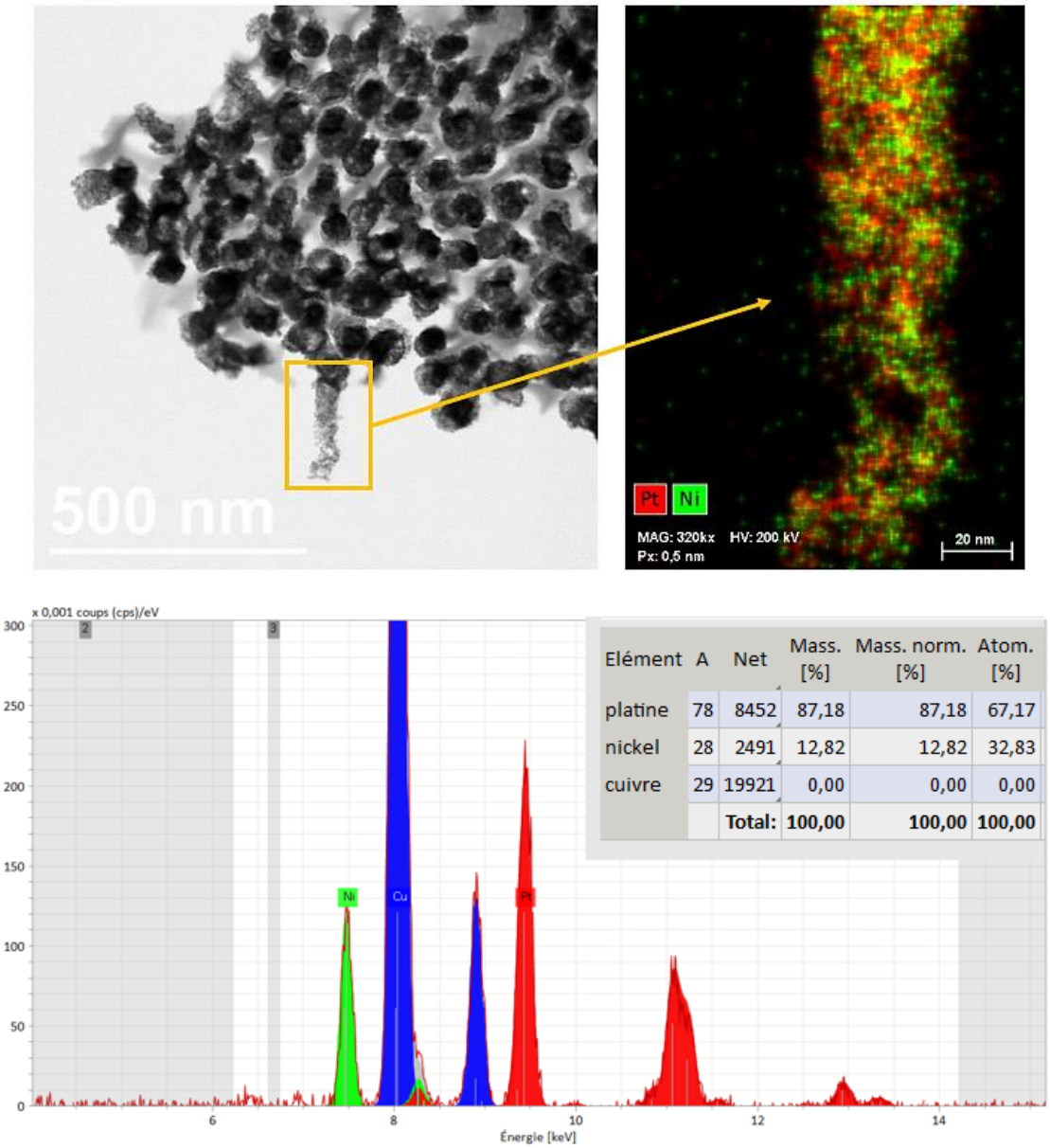

Elément	A	Net	Mass. [%]	Mass. norm. [%]	Atom. [%]
platine	78	8452	87,18	87,18	67,17
nickel	28	2491	12,82	12,82	32,83
cuivre	29	19921	0,00	0,00	0,00
		Total:	**100,00**	**100,00**	**100,00**

Figure S18. Representative TEM-coupled EDX analysis of Pt_2NiNWs prepared after exposing NiNWs to a K_2PtCl_4 solution in 0.05 M HCl at 35°C for 8 minutes.

The sample was further characterized by X-ray diffraction (XRD) in order to investigate the crystalline structure of the metal phases. Measurements were performed via a Bruker D8 diffractometer equipped with a Cu-Kα source (λ = 0.15406 nm). The offset coupled θ-2θ mode was used to avoid the strong Si(400) reflection of the support.

According to the XRD pattern obtained in *figure S19* below, peaks are shifted to higher 2θ values with respect to pure Pt due to the solid solution formation. Shifted peaks positioned at 2θ values of 40.2º, 46.8º and 82.4º correspond to the (111), (200) and (311) reflections of the face-centered cubic (fcc) crystal lattice of $Pt_{1-x}Ni_x$. For comparison, the pure fcc Pt peaks are positioned at 2θ values 39.8º, 46.2º and 81.3º. The (220) PtNi peak is not visible because it is

hidden by a signal coming from the (400) reflection of the Si support. As displayed in the XRD pattern, no characteristic peaks indicating the existence of Ni or NiO crystal structures are detected. For this sample, the lattice parameter was found to be 3.88 Å, which corresponds to a solid solution alloy $Pt_{1-x}Ni_x$ with x = 0,14.

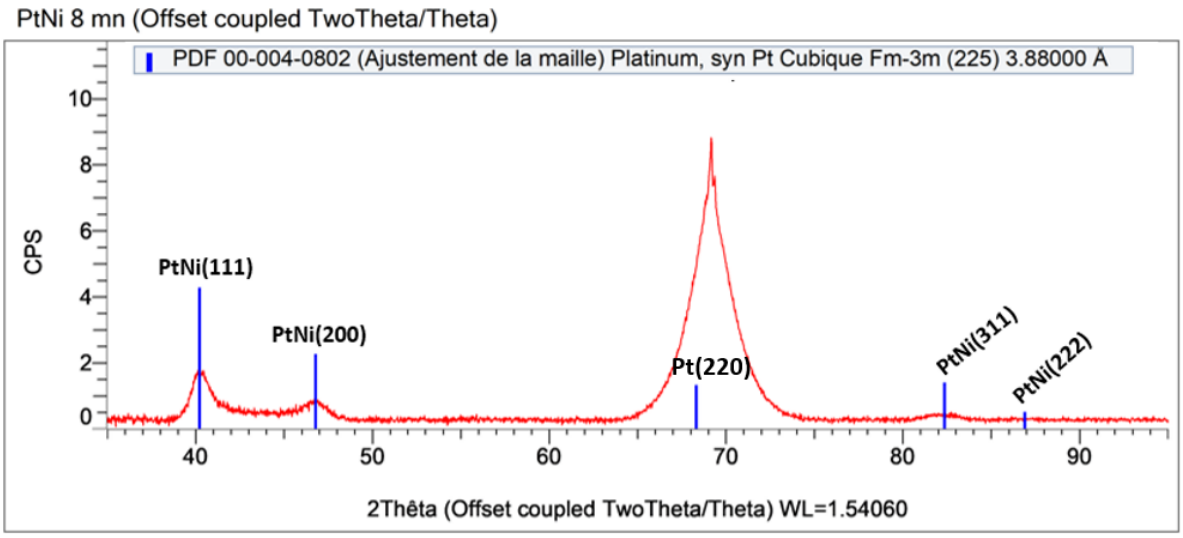

Figure S19. XRD measurements performed on the as-prepared PtNiNWs supported on p-Si(100).

The PtNiNWs will be directly transferred into the ionomer membrane by hot-pressing. The surface roughness of the outer surface of the nanowires could be related to the vacancies formed by the dissolution of Ni.

PtNiNTs fabrication:

The elaboration of PtNiNTS has followed a different process. After the etching of the AAO in 5%wt orthophosphoric solution at 35°C, self-standing nanowires attached to Si substrate were dipped in a 1mM K_2PtCl_4 solutions different temperatures ranging from 60° to 90°C for 1 to 8 hours. Exposure time to Pt salt solution has been investigated, as shown in *figure S20* below.

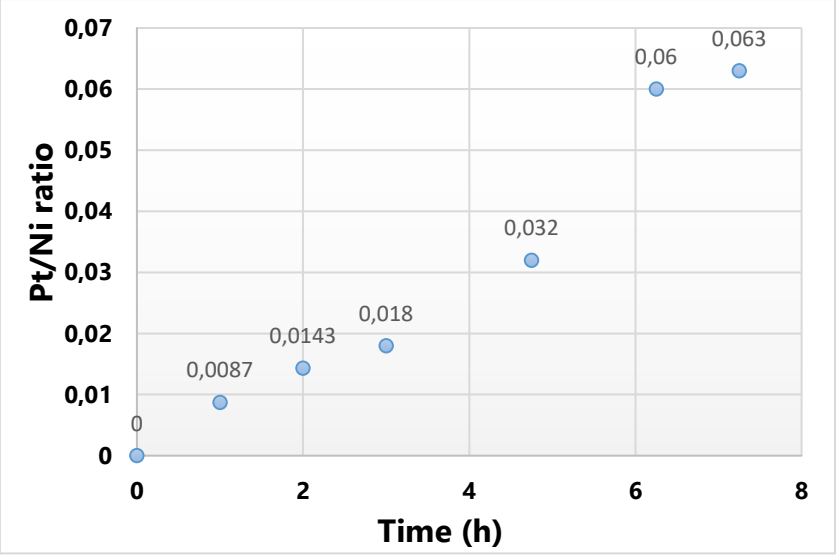

Figure S20: The evolution of the Pt/Ni atomic ratio obtained from EDX analysis during the GD reaction over time in 10^{-3}M K_2PtCl_4 solution at 60°C.

Elemental integrated EDX spectrum was used for semi-quantitative composition estimation (*figure S21*below) and showed an increase in the Pt/Ni atomic ratio over exposure time.

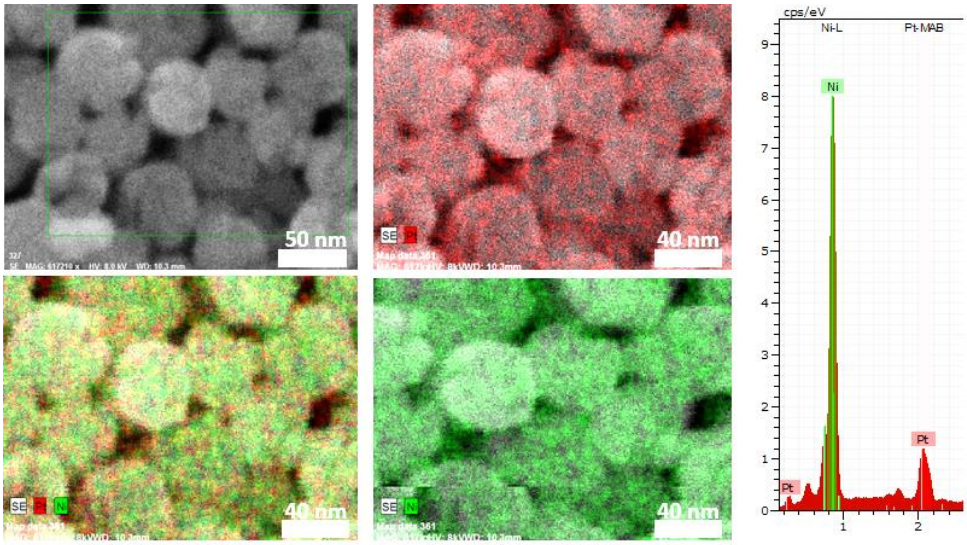

Figure S21. SEM-EDX elemental mapping of the top of the PtNi nanowires after exposing the sample to a K_2PtCl_4 solution at 60°C for 5 hours.

A thin layer of Pt was deposited around the NiNWs which might refer to whether a reduction or the deposit of the Pt salt. As we will see later, this layer consists of an oxide layer surrounding the NiNWs.

Measurements were performed via a Bruker D8 diffractometer equipped with a Cu-Kα source (λ = 0.15406 nm) using the offset coupled θ-2θ mode.

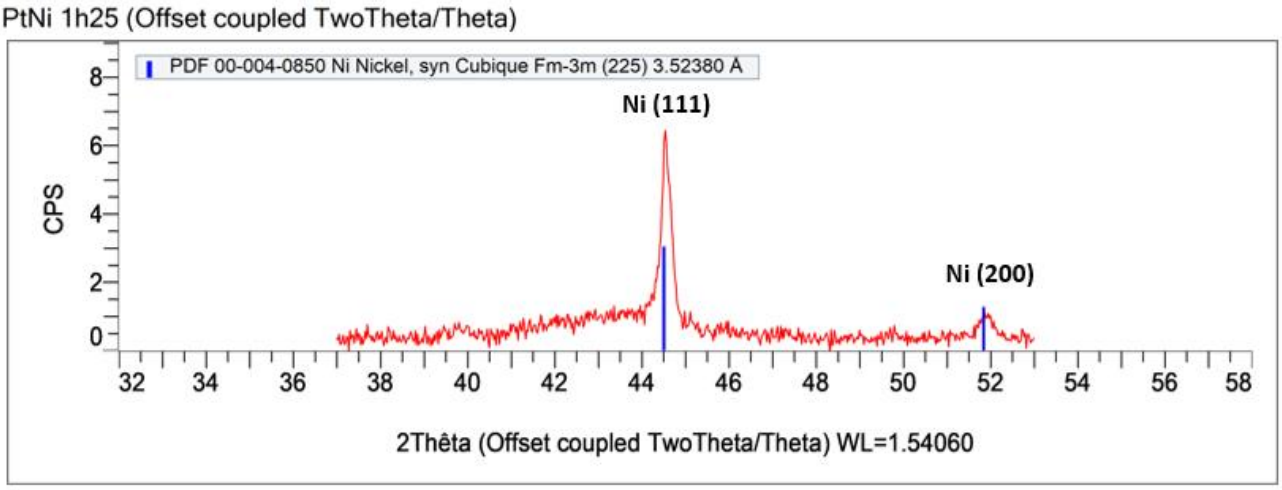

Figure S22: XRD measurements performed on PtNiNWs at low Pt deposition where Ni peaks are clearly visible. PtNi nanowires were obtained after exposing the NiNWs sample to a K_2PtCl_4 solution at 80°C for 1.5 hours.

The *figure S23* below displays the elemental EDX map for the PtNiNTs on Nafion® membrane after Acid Leaching in H_2SO_4 0.5M at 35°C.

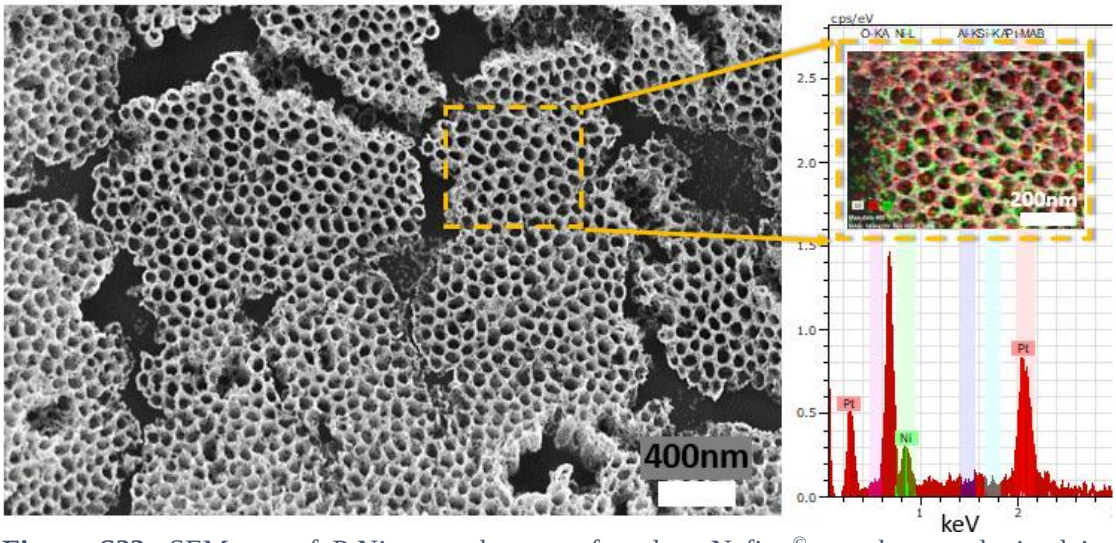

Figure S23: SEM top of PtNi nanotubes transferred to Nafion© membrane, obtained in a non-confined system in K_2PtCl_4 solution heated to 80°C for 1.5 hours. After GD, the PtNiNWs were heated under H_2/Ar atmosphere for 2 hours at 250°C. After that, PtNiNWs were transferred to the Nafion© membrane by a hot-pressing process followed by an acid-leaching process in a sulfuric acid solution. According to the EDX quantitative analysis, the atomic ratio of Pt:Ni is 3:1.

XRD experiments were performed on PtNiNTs embedded onto the Nafion® membrane sample:

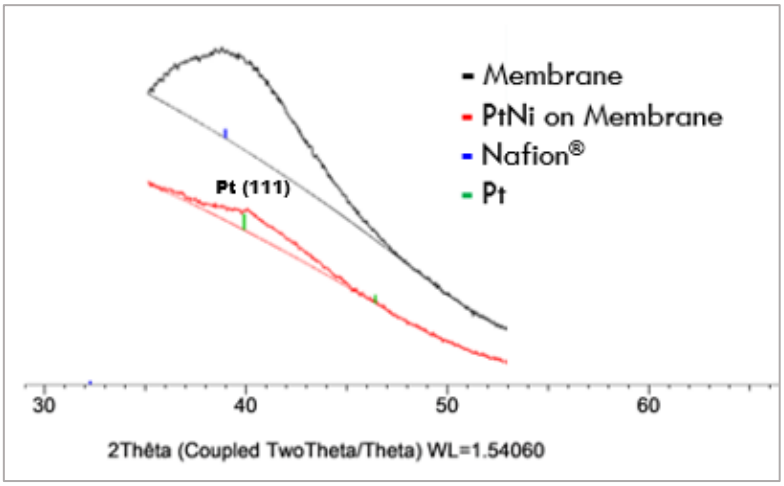

Figure S24: XRD measurements performed on PtNiNTs embedded onto the Nafion® membrane.

SI 10: *Table S4* below contextualizes a brief review of the properties of each MEA tested in this work before and after aging. The values of specific surface after AST is calculated considering the Pt loading before AST.

	$I_s^{0.8V\ iR\text{-}free}$ (A/cm^2_{Pt})	$I_m^{0.8V\ iR\text{-}free}$ (A/g_{Pt})	Roughness (cm^2_{Pt}/cm^2_{geo})	S_{Pt} (cm^2_{Pt})	ECSA (m^2/g_{Pt})	Loading before AST ($\mu g_{Pt}/cm^2$)
Pt/C Before	7.0×10^{-3}	1475	7.3	13	21	35
Pt/C After	3.3×10^{-3}	41	0.6	1	1.7	
PtNiNWs Before	9.7×10^{-2}	1992	6.8	2	7	100
PtNiNWs After	1.5×10^{-2}	261	5.8	1.7	6	
PtNiNTs Before	4×10^{-3}	983	3.7	0.6	25	15
PtNiNTs After	1.1×10^{-2}	1225	1.8	0.3	12	
Pt_3Ni_7/NSTF*	1.3×10^{-2}	2000	18.75	-	15	125

Table S4: Summary of activities, ECSA, roughness, platinum surface, and Pt-loading of each tested cathode: Pt/C, PtNiNWs, and PtNiNTs, at 80°C, 100%RH, 1.5 bar, under O_2. *For NSTF, at 80°C, 60%RH, 1.5 bar, under Air.

SI 11: Polarization curves realized under H_2/Air and H_2/O_2:

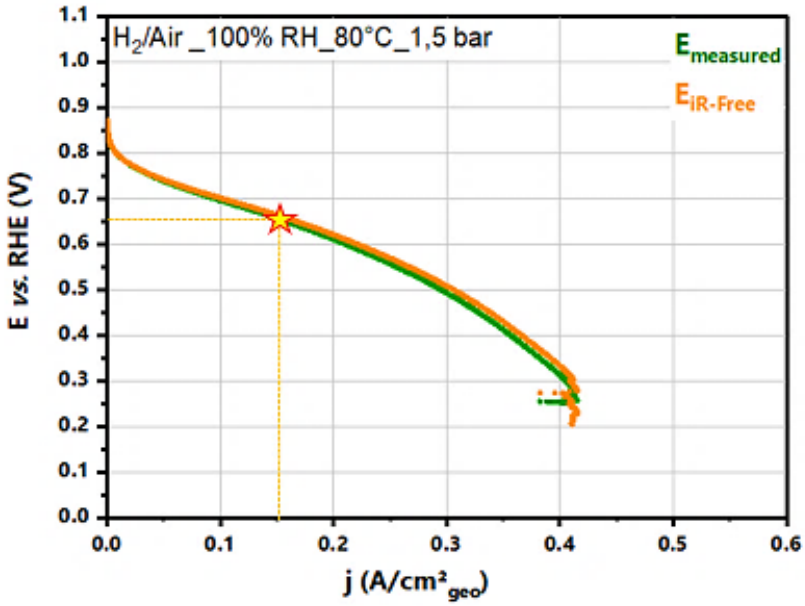

Figure S25: Measured polarization curve for **Pt/C** electrode as a function of geometrical current density at T_{cell}=80°C, 100% RH (dew points), wet H_2/Air-gas flow, and a total pressure of 1.5 bar. Green-curve: original un-corrected polarization curve, and Orange-curve: The resistance-corrected cell voltage ($E_{iR\text{-}free}$).

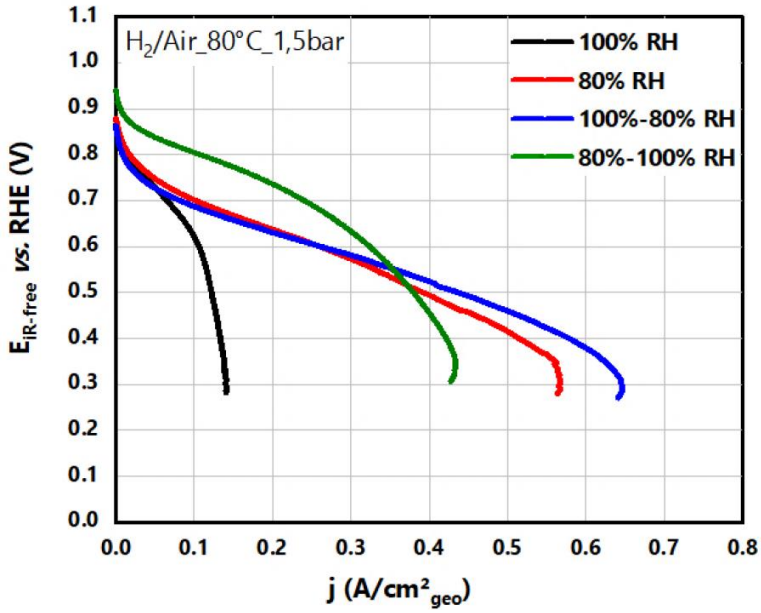

Figure S26: Fuel cell's polarization curves (corrected from ohmic drop) of **PtNiNWs** cathodes at operating conditions in the order of anode/cathode: H_2/Air, cell temperature of 80°C, at different relative humidity values and a total pressure of 1.5 bar, 1.38 bar, 1.38-1.5 bar, and 1.5-1.38 bar at 100% RH, 80% RH, 80%-100% RH, and 100%-80% RH, respectively.

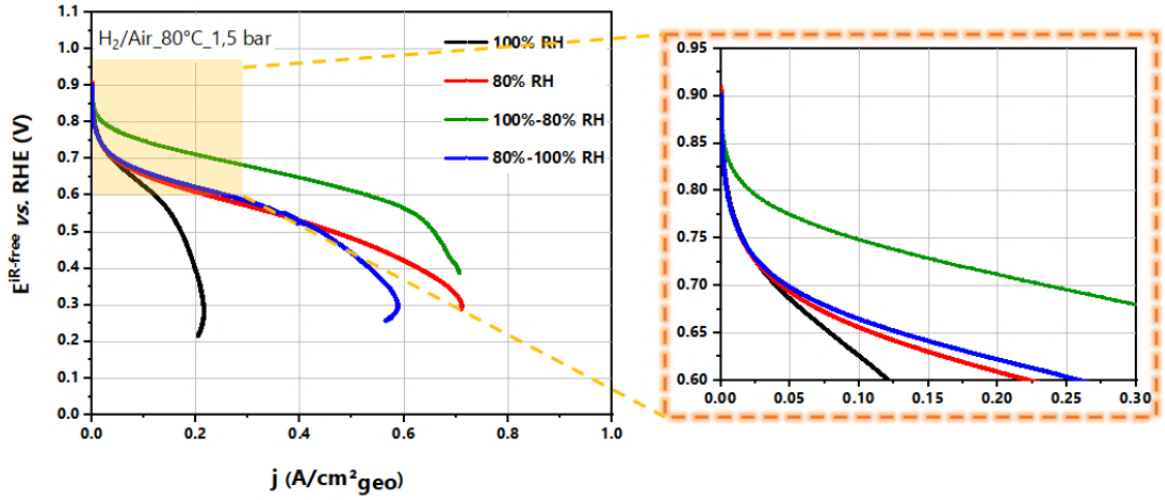

Figure S27: Comparison of fuel cell's ohmically-corrected polarization curves of **PtNiNTs** cathodes at operating conditions in the order of anode/cathode in H_2/Air, a cell temperature of 80°C, at different relative humidity values and a total pressure of 1.5 bar, 1.38 bar, 1.38-1.5 bar, and 1.5-1.38 bar at 100% RH, 80% RH, 80%-100% RH, and 100%-80% RH, respectively.

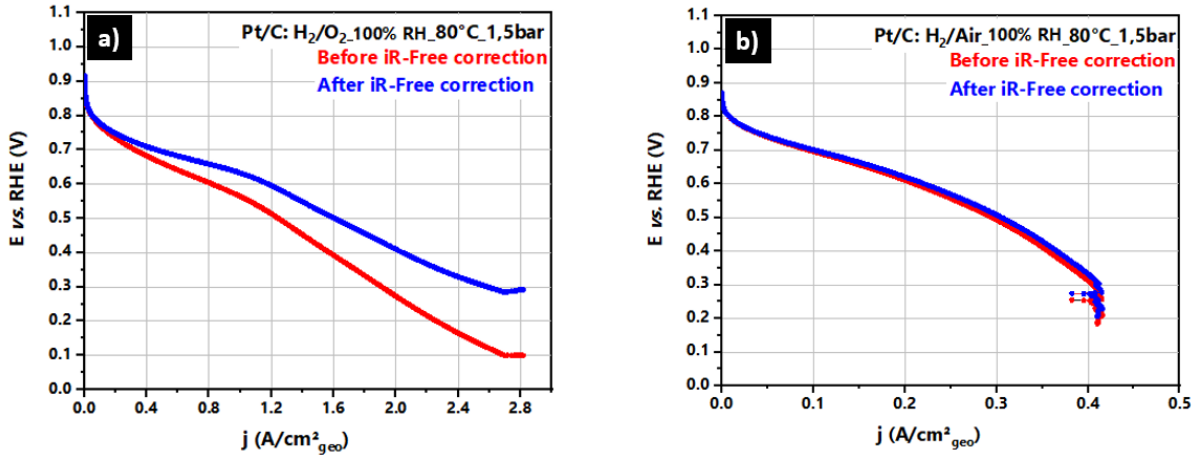

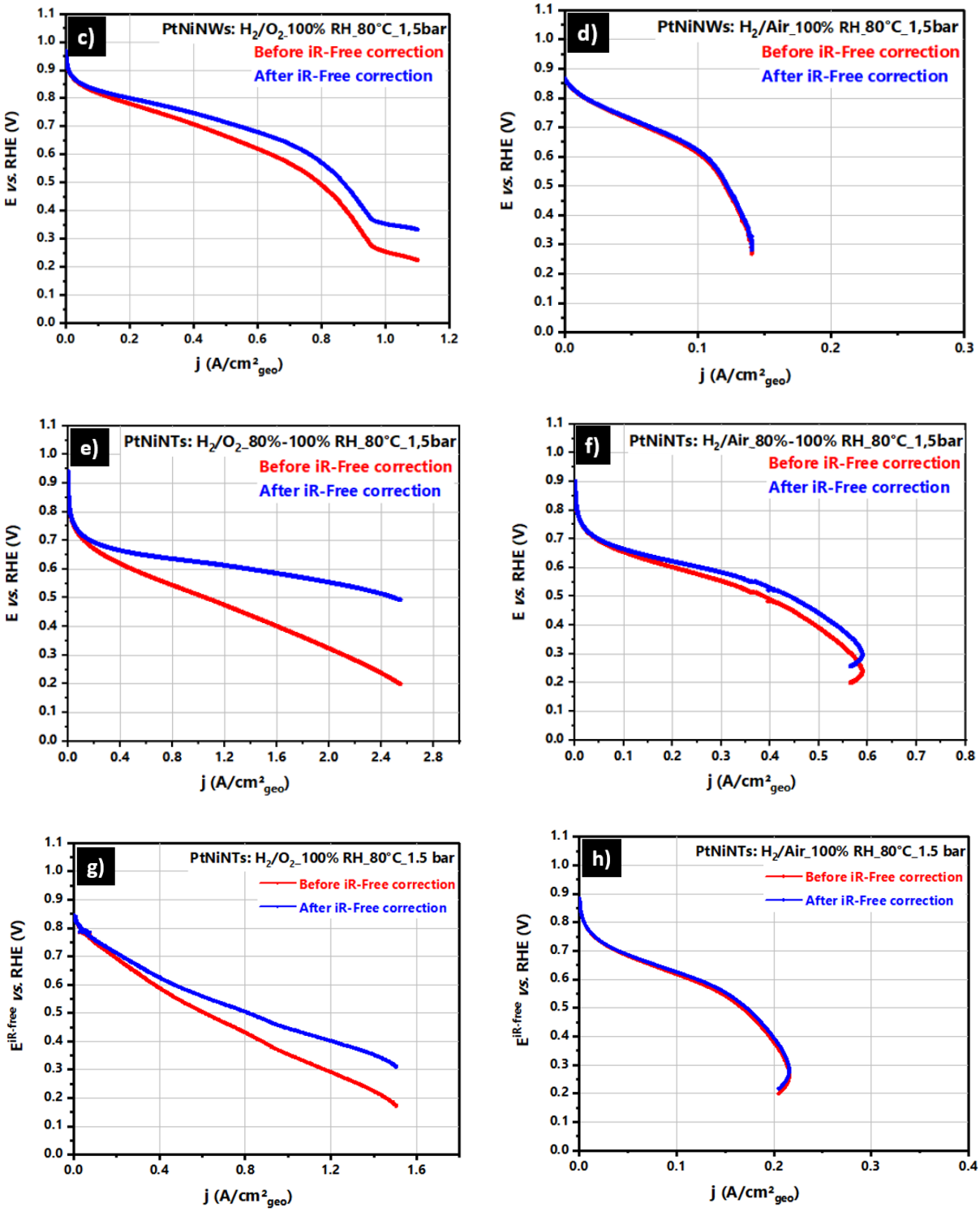

Figure S28: Comparison of fuel cell's polarization curves before and after iR-free correction of **a-b)** Pt/C, **c-d)** PtNiNWs, and **e-h)** PtNiNTs cathodes at operating conditions in the order of anode/cathode in H_2/O_2 and H_2/Air, a cell temperature of 80°C, at 1.5 bar. Relative humidity was fixed at 100%RH for Pt/C and PtNiNWs, and 100%RH and 80-100%RH for PtNiNTs.

References

[1] K. Nielsch, J. Choi, K. Schwirn, R.B. Wehrspohn, U. Gösele, Self-ordering Regimes of Porous Alumina: The 10 Porosity Rule, Nano Lett. 2 (2002) 677–680.

[2] J. Descarpentries, D. Buttard, L. Dupré, T. Gorisse, Highly conformal deposition of copper nanocylinders uniformly electrodeposited in nanoporous alumina template for ordered catalytic applications, Micro & Nano Letters. 7 (2012) 1241–1245.

[3] M. Zhiani, S. Majidi, Effect of MEA conditioning on PEMFC performance and EIS response under steady state condition, International Journal of Hydrogen Energy. 38 (2013) 9819–9825.

[4] S.M. Alia, C. Ngo, S. Shulda, M.-A. Ha, A.A. Dameron, J.N. Weker, K.C. Neyerlin, S.S. Kocha, S. Pylypenko, B.S. Pivovar, Exceptional Oxygen Reduction Reaction Activity and Durability of Platinum–Nickel Nanowires through Synthesis and Post-Treatment Optimization, ACS Omega. 2 (2017) 1408–1418.